J Adv Ceram

Research Article

Two-step solid-state synthesis of 413 high-purity high-entropy MAX phases based on the structural genetic mechanism and investigation of their microwave absorption performance

Chengjiao Che[1,2], Lintao Liu[1,2], Tan Shi[1,2], Hongyi Wang[1,2], Yiming Li[1,2], Dong Wang[3], Hongyu Gong[1,2], Jianqiang Bi[1,2,✉], Xihua Zhang[2,4,✉]

Cite this article: Che C, Liu L, Shi T, et al. *J Adv Ceram* 2026, **15**(8): 9221350. https://doi.org/10.26599/JAC.2026.9221350

ABSTRACT: The difficult synthesis and low purity of 413 high-entropy MAX phase powders have severely constrained their development in the field of electromagnetic wave absorption. To address this, the present study optimized a two-step solid-phase synthesis process. By examining how different raw-material pretreatment methods affect the structural evolution of carbide precursors, we proposed a "structural genetic mechanism" that systematically explains the synthesis pathway of the 413 high-entropy MAX phase. The results show that cubic-phase carbide precursors are essential for producing 413 high-purity high-entropy MAX. Using the optimized method, we synthesized pure-phase 413 high-entropy MAX and, for the first time, successfully prepared $(Mo_{0.2}Ta_{0.2}Nb_{0.2}Ti_{0.2}V_{0.2})_4AlC_3$ via a conventional pressureless solid-state reaction route. Wave absorption tests indicate that the synthesized 413 high-entropy MAX phases all exhibit good absorption performance. In particular, $(Mo_{0.2}Cr_{0.2}Nb_{0.2}Ti_{0.2}V_{0.2})_4AlC_3$ achieved a maximum effective absorption bandwidth (EAB_{max}) of 4.24 GHz at a thickness of 1.57 mm and a minimum reflection loss (RL_{min}) of −52.88 dB at 1.87 mm. $(Mo_{0.2}Ta_{0.2}Nb_{0.2}Ti_{0.2}V_{0.2})_4AlC_3$ showed a clear advantage at small thicknesses, with an EAB_{max} of 3.44 GHz at 0.93 mm and an RL_{min} of −51.60 dB at 0.89 mm. This study fully demonstrated the effective regulation of wave absorption performance by high-entropy engineering and provided an effective approach to expand the types of 413 high-entropy MAX phase powders, offering a useful reference for exploring this material in the field of wave absorption.

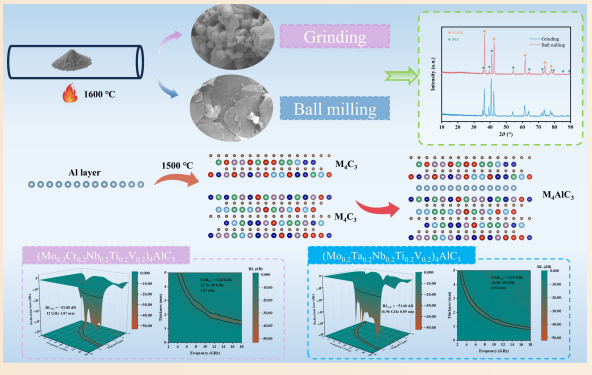

KEYWORDS: high entropy; MAX phase; microwave absorption; lattice distortion

1 Introduction

Electromagnetic-wave absorbing materials reduce environmental electromagnetic pollution, protect electronic components, and lower the health risks of electromagnetic radiation [1,2]. High-performance absorbers should be strong, broadband, thin, and lightweight. In many industrial and military settings, they also require high-temperature stability, oxidation resistance, and corrosion resistance [3,4]. Against this backdrop, MAX-phase materials have shown great potential for electromagnetic-wave absorption because of their layered crystal structure and favorable physical and chemical properties [5,6].

MAX phases are ternary carbides or nitrides with a layered hexagonal structure. Their general formula is $M_{n+1}AX_n$ (M is a pre-transition metal, A is mainly a Group IIIA or IVA element, and X is C or N), with n typically equal to 1, 2, or 3 (corresponding to 211, 312, and 413 phases). Their crystal structure consists of alternating M_6X octahedral layers and A-element layers. M_6X denotes an octahedral coordination unit, in which one X atom is located at the center of the octahedron and is coordinated by six surrounding M atoms [7]. Traditional single-component MAX phases offer high-temperature stability and oxidation resistance but exhibit poor microwave absorption. For example, the Cr_2AlC studied by Zhang *et al.* [8] showed a minimum reflection loss (RL_{min}) of −25.09 dB and a maximum effective absorption bandwidth (EAB_{max}) of only 2.2 GHz, which is attributable to a single loss mechanism. Introducing the high-entropy concept into MAX phases creates high-entropy MAX phases in which multiple metal species occupy the M site in solid solution; these phases

[1] Key Laboratory for Liquid-Solid Structural Evolution and Processing of Materials, Ministry of Education, Shandong University, Jinan 250061, China. [2] School of Materials Science and Engineering, Shandong University, Jinan 250061, China. [3] Shandong Huamei New Mat Technol Co., Ltd., Weifang 261200, China. [4] Schools of Future Technology, Shandong University, Jinan 250061, China.

✉ Corresponding authors. E-mail: J. Bi, bjq1969@163.com; X. Zhang, zhangxh@sdu.edu.cn

Received: May 11, 2026; Revised: July 3, 2026; Accepted: July 13, 2026

retain the intrinsic oxidation resistance and high-temperature stability while offering expanded opportunities to enhance microwave absorption via multicomponent synergistic effects [9,10]. Shen *et al.* [11] prepared $(Ti_{0.2}Zr_{0.2}V_{0.2}Nb_{0.2}Ta_{0.2})_2AlC$ and reported an RL_{min} of −47 dB and an EAB_{max} of 3.92 GHz. Qiao *et al.* [12] synthesized $(Mo_{0.25}Cr_{0.25}Ti_{0.25}V_{0.25})_3AlC_2$ and observed an RL_{min} of −45.8 dB with an EAB_{max} of 3.6 GHz. These studies indicate that high-entropy engineering is an effective approach to improving the absorption performance of MAX phases. The mechanism is that lattice distortion, defects, and uneven charge distribution introduced by multiple elements occupying the M site promote the formation of electric dipoles, thereby enhancing the material's polarization loss. Therefore, in theory, 413 high-entropy MAX phases should exhibit superior and more controllable microwave-absorption performance because of increased M-layer stacking. However, few reports currently address 413 high-entropy MAX phases, mainly because their synthesis is extremely challenging [13,14]. Among the experimentally synthesized traditional MAX phases, more than eighty have been produced: over fifty are 211 phases, more than twenty are 312 phases, and only twelve are 413 phases [15]. For high-entropy MAX phases, only approximately a dozen types have been synthesized experimentally to date, and most belong to the 211 family [16–20]. Moreover, most existing studies have used pressure-assisted techniques such as hot-press sintering [21] or spark plasma sintering [22,23], which promote solid-solution formation among different elements through applied pressure. These methods primarily yield bulk products and, therefore are unsuitable for the large-scale powder production required for wave-absorption applications. Solid-state synthesis is an effective route for producing MAX powders efficiently, but it poses substantial challenges for preparing high-entropy MAX powders. In 2021, $MoCrTiVAlC_3$ and $MoNbTiVAlC_3$ were synthesized by a solid-state route for the first time; however, the products contained significant carbide and alloy impurities [24]. In 2023, $(Mo_{0.2}Cr_{0.2}Nb_{0.2}Ti_{0.2}V_{0.2})_4AlC_3$ was synthesized for the first time, but it likewise contained alloy and alumina impurities [25]. In 2025, Wyatt *et al.* [26] reported a series of 413 high-entropy MAX phases; however, their phase purity was generally low, accompanied by a significant presence of carbides and alloy byproducts. In certain systems, the characteristic (002) diffraction peaks indicative of the layered structure of the 413-MAX phase were completely absent. Only $(Ti_{0.2}V_{0.2}Nb_{0.2}Ta_{0.2}W_{0.2})_4AlC_3$ and $(Ti_{0.2}V_{0.2}Mo_{0.2}Ta_{0.2}W_{0.2})_4AlC_3$ exhibited relatively high phase purity. To date, no studies have documented the preparation of the new 413 high-entropy MAX phase using the solid-phase method. Consequently, achieving high-purity preparation of the 413 high-entropy MAX phase and further enriching its component design has emerged as a critical issue that limits its in-depth research and application in the field of electromagnetic wave absorption. To date, no reports have described the solid-state synthesis of new 413 high-entropy MAX phases. Therefore, efficiently preparing and expanding the 413 high-entropy MAX system has become a key challenge that limits its development in the wave-absorption field.

To address this, we adopted an improved two-step solid-state route to prepare pure-phase 413 high-entropy MAX powders and examined their phase evolution and synthesis mechanism using two raw-material pretreatment methods: grinding and ball milling. Using this approach, we successfully synthesized a novel 413 high-entropy MAX composition, $(Mo_{0.2}Ta_{0.2}Nb_{0.2}Ti_{0.2}V_{0.2})_4AlC_3$, which demonstrates the method's generality. Wave-absorption tests show that powders produced by this route exhibit excellent absorption performance. In particular, $(Mo_{0.2}Cr_{0.2}Nb_{0.2}Ti_{0.2}V_{0.2})_4AlC_3$ achieved an RL_{min} of −52.88 dB and an EAB_{max} of 4.24 GHz. The matching thickness corresponding to the maximum absorption bandwidth of $(Mo_{0.2}Ta_{0.2}Nb_{0.2}Ti_{0.2}V_{0.2})_4AlC_3$ was only 0.93 mm, fully demonstrating that the high-entropy cocktail effect can effectively tune the absorption properties. This work provides an effective approach to expand the family of 413 high-entropy MAX powders and paves the way for exploring these materials in wave-absorption applications.

2 Experimental

2.1 Raw materials

The following materials were used in this experiment: Mo (≥ 99.9% metals basis), Cr (≥ 99.5% metals basis), Nb (≥ 99.5% metals basis), Ti (≥ 99.9% metals basis), V (≥ 99.5% metals basis), Ta (≥ 99.9% metals basis), Al (≥ 99.5% metals basis), and graphite powder (≥ 99.95% metals basis), all purchased from Shanghai Aladdin Biochemical Technology Co., Ltd.

2.2 Synthesis of high-entropy carbides

In this study, high-entropy carbides served as precursors for synthesizing high-entropy MAX phases, and we investigated how raw-material pretreatment methods (grinding and ball milling) affected phase evolution. First, metal powders for the M site and graphite were weighed according to the stoichiometric ratio. For example, for $(Mo_{0.2}Cr_{0.2}Nb_{0.2}Ti_{0.2}V_{0.2})_4AlC_3$, the components were mixed at a molar ratio of Mo : Cr : Nb : Ti : V : C = 0.8 : 0.8 : 0.8 : 0.8 : 0.8 : 2.7. The carbon content was set to 2.7 to introduce an appropriate level of carbon vacancies to promote the formation of the subsequent MAX phase [27]. Next, the mixed powders underwent pretreatment in anhydrous ethanol. For the grinding group, powders were ground in an agate mortar for 30 min to ensure macroscopic uniformity. For the ball-milling group, a ball-to-material ratio of 5 : 1 and a rotational speed of 350 r/min were used for 12 h. The resulting slurry was dried with forced air at 60 °C and then pressed into green bodies at 30 MPa. The green bodies were heated in a tube furnace to 1600 °C at 5 °C/min under an argon atmosphere and held for 3 h. After furnace cooling to room temperature, the high-entropy carbide precursors were retrieved and crushed. The prepared carbides were denoted MCTV-C, MNTV-C, MCNTV-C, and MTNTV-C for $(Mo_{0.25}Cr_{0.25}Ti_{0.25}V_{0.25})_4C_{2.7}$, $(Mo_{0.25}Nb_{0.25}Ti_{0.25}V_{0.25})_4C_{2.7}$, $(Mo_{0.2}Cr_{0.2}Nb_{0.2}Ti_{0.2}V_{0.2})_4C_{2.7}$, and $(Mo_{0.2}Ta_{0.2}Nb_{0.2}Ti_{0.2}V_{0.2})_4C_{2.7}$, respectively. To distinguish between different processing methods, grinding and ball milling are denoted G and BM, respectively. For example, the $(Mo_{0.25}Cr_{0.25}Ti_{0.25}V_{0.25})_4C_{2.7}$ carbide precursor prepared by grinding was denoted G-MCTV-C.

2.3 Synthesis of 413 high-entropy MAX phases

The high-entropy carbides prepared above served as precursors for synthesizing the target 413 high-entropy MAX phases via a solid-solution reaction with aluminum powder. Using $(Mo_{0.2}Cr_{0.2}Nb_{0.2}Ti_{0.2}V_{0.2})_4Al_xC_{2.7}$ as an example, the MCNTV-C precursor and aluminum powder were weighed in a molar ratio of 1 : x. Literature indicates that an excess of Al (x = 1.2) is typically added to compensate for Al volatilization at high temperatures [28]. However, our preliminary experiments showed that an Al addition of 1.2 did not produce the 413 high-entropy MAX phase. Therefore, this study performed a gradient optimization of the Al addition to investigate its influence on phase evolution and phase purity. The weighed mixed powder was placed in an agate mortar with anhydrous ethanol and ground thoroughly. After the slurry dried, it was pressed into a green body under 30 MPa. The green

body was then heated in a tube furnace to 1500 °C at 5 °C/min under an argon atmosphere and held for 1 h. After the reaction was completed, the product was cooled to room temperature in the furnace and ground into powder. To distinguish the precursor processing methods, elemental systems, and Al contents, the high-entropy MAX phase samples were uniformly denoted G/BM-M-A_x, where G and BM represent grinding and ball milling treatments, respectively; M denotes the M-site metal elemental system and is abbreviated using the initials of the constituent elements; and A_x represents the stoichiometric coefficient of Al. For example, G-MCTV–$A_{1.6}$ refers to the $(Mo_{0.25}Cr_{0.25}Ti_{0.25}V_{0.25})_4Al_{1.6}C_{2.7}$ high-entropy MAX phase sample prepared from the $(Mo_{0.25}Cr_{0.25}Ti_{0.25}V_{0.25})_4C_{2.7}$ carbide precursor treated by grinding. The detailed sample nomenclature is provided in Table S1 in the Electronic Supplementary Material (ESM).

2.4 Characterizations

Phase identification was performed using an X-ray diffractometer (XRD; DMAX-2500PC, Rigaku). The sample morphology was examined by a field-emission scanning electron microscope (FE-SEM; Gemini 500, ZEISS) and a transmission electron microscope (TEM; JEM-F200, JEOL). The crystal structure was analyzed by high-resolution transmission electron microscopy (HRTEM) and selected area electron diffraction (SAED). Surface element valence states and bonding characteristics were examined by an X-ray photoelectron spectrometer (XPS; AXIS SUPRA, Shimadzu). Finally, the complex dielectric constant (ε_r) and complex permeability (μ_r) of the samples in the 2–18 GHz frequency band were measured by the coaxial method using a vector network analyzer (VNA; Agilent N1500A). The optimized filler loadings of $(Mo_{0.25}Cr_{0.25}Ti_{0.25}V_{0.25})_4AlC_3$, $(Mo_{0.25}Nb_{0.25}Ti_{0.25}V_{0.25})_4AlC_3$, $(Mo_{0.2}Cr_{0.2}Nb_{0.2}Ti_{0.2}V_{0.2})_4AlC_3$, and $(Mo_{0.2}Ta_{0.2}Nb_{0.2}Ti_{0.2}V_{0.2})_4AlC_3$ are 75, 75, 70, and 80 wt%, respectively. These filler loadings were selected because this work aims to evaluate the best achievable microwave absorption performance of each MAX phase system under optimized loading conditions. Specifically, for each MAX phase system, the microwave absorption performance was systematically investigated within the loading range of 65–80 wt% at an interval of 5 wt%, namely, 65, 70, 75, and 80 wt%. The absorption performances of the other filler loadings for each system are provided in Fig. S1 in the ESM, which supports the determination of the optimized loading for each MAX phase sample.

2.5 Radar cross-section (RCS) simulation

The RCS simulations were performed using CST Studio Suite. The radar cross-section module was employed, and the integral equation solver was selected for the calculations. The mesh was generated using the automatic surface meshing scheme of the integral equation solver. The simulation model consisted of a 180 mm × 180 mm perfect electric conductor (PEC) substrate coated with an absorber layer of the corresponding thickness. Open boundary conditions were applied to simulate the far-field scattering environment. The RCS results were obtained through angular scanning, where θ was swept from −90° to 90°, φ was fixed at 90°, and the angular step was set to 1°.

3 Results and discussion

3.1 Structure characterization

Figures 1(a) and 1(d) illustrate the XRD patterns of the MCTV-C and MCNTV-C precursors, which were prepared using grinding and ball-milling mixing processes, respectively. The results indicate that the pretreatment method significantly influences the phase composition of carbide solid solutions at elevated temperatures. As shown in Figs. 1(b) and 1(e), the samples subjected to grinding pretreatment mainly exhibit the characteristics of hexagonal carbides. Specifically, the contents of hexagonal carbides in G-MCTV–C and G-MCNTV–C are 65.79 and 50.54 wt%, respectively. In contrast, as shown in Figs. 1(c) and 1(f), the ball-milled samples are dominated by cubic carbides, with cubic carbide contents of 73.33 and 55.80 wt% in BM-MCTV-C and BM-MCNTV-C, respectively. These results indicate that ball milling promotes the formation of cubic carbide precursors, whereas grinding tends to favor the formation of hexagonal carbide phases. This variation in phase selectivity arises from the intense mechanical activation effect generated during the ball-milling process. As depicted in Figs. 1(n) and 1(o), the powder resulting from manual grinding retains its original blocky characteristics, with a limited contact interface. Conversely, the ball-milling process facilitates the formation of an interwoven thin flaky structure within the powder. This morphological transformation substantially increases the contact area of the reaction interface and shortens the diffusion distance between components, thereby facilitating interdiffusion and promoting the formation of cubic carbide solid-solution precursors. In the preparation of the MAX phase, an excess of Al_x (x = 1.2) is typically added to compensate for volatilization losses at elevated temperatures. However, preliminary experiments confirm that for the 413 high-entropy MAX phases, an addition of 1.2 is inadequate. Therefore, we conducted a gradient optimization of the Al addition amount. As illustrated in Fig. 1(g), the G-MCTV–C synthesized through grinding, even with an optimized aluminum content of Al = 2.2, still exhibits significant amounts of M_3AX_2 and carbide impurities. The G-MCNTV–C produced by the grinding process (Fig. 1(i)) lacks M_3AX_2; however, it still shows the presence of carbide impurities and diffraction peak splitting, indicating that the purity of the 413 high-entropy MAX phases derived from the hexagonal carbide precursor remains inadequate. For the BM-MCTV-C and BM-MCNTV-C samples prepared via ball milling (Figs. 1(h) and 1(j)), an increase in aluminum content leads to a gradual transformation of cubic carbides into the M_4AX_3 phase. At Al = 2.0, the 413 high-purity high-entropy MAX phase was successfully synthesized, with no impurity phases detected within the detection limit of XRD. This notable phase selectivity underscores the critical role of the "structural genetic mechanism" in the two-step synthesis of the 413 high-entropy MAX phase. As shown in Fig. 1(p), the $P6_3/mmc$-type hexagonal carbide precursor viewed along the [0001] direction exhibits an ABAB stacking sequence, and its M–C octahedral connectivity is different from that of the M_4AX_3 phase. In contrast, the $Fm\bar{3}m$-type cubic carbide precursor viewed along the [111] direction shows close-packed {111} planes that have better crystallographic matching with the (0001) basal planes of the M_4AX_3 phase. Such structural compatibility is favorable for the insertion of Al atoms between adjacent M_4C_3 layers, thereby promoting the formation of high-purity M_4AX_3 phases. In contrast, the hexagonal carbide precursor requires more substantial rearrangement of the stacking sequence, making its transformation into the M_4C_3 phase less favorable. To accurately characterize the crystal structure of the synthesized materials, we conducted Rietveld refinement on BM-MCTV-$A_{2.0}$ and BM-MCNTV-$A_{2.0}$ (Figs. 1(k) and 1(l)). The refined results align well with the V_4AlC_3 structural model. The refined unit cell parameters are presented in Table S2 in the ESM. As the number of components increases, the unit cell parameters of BM-MCTV-$A_{2.0}$

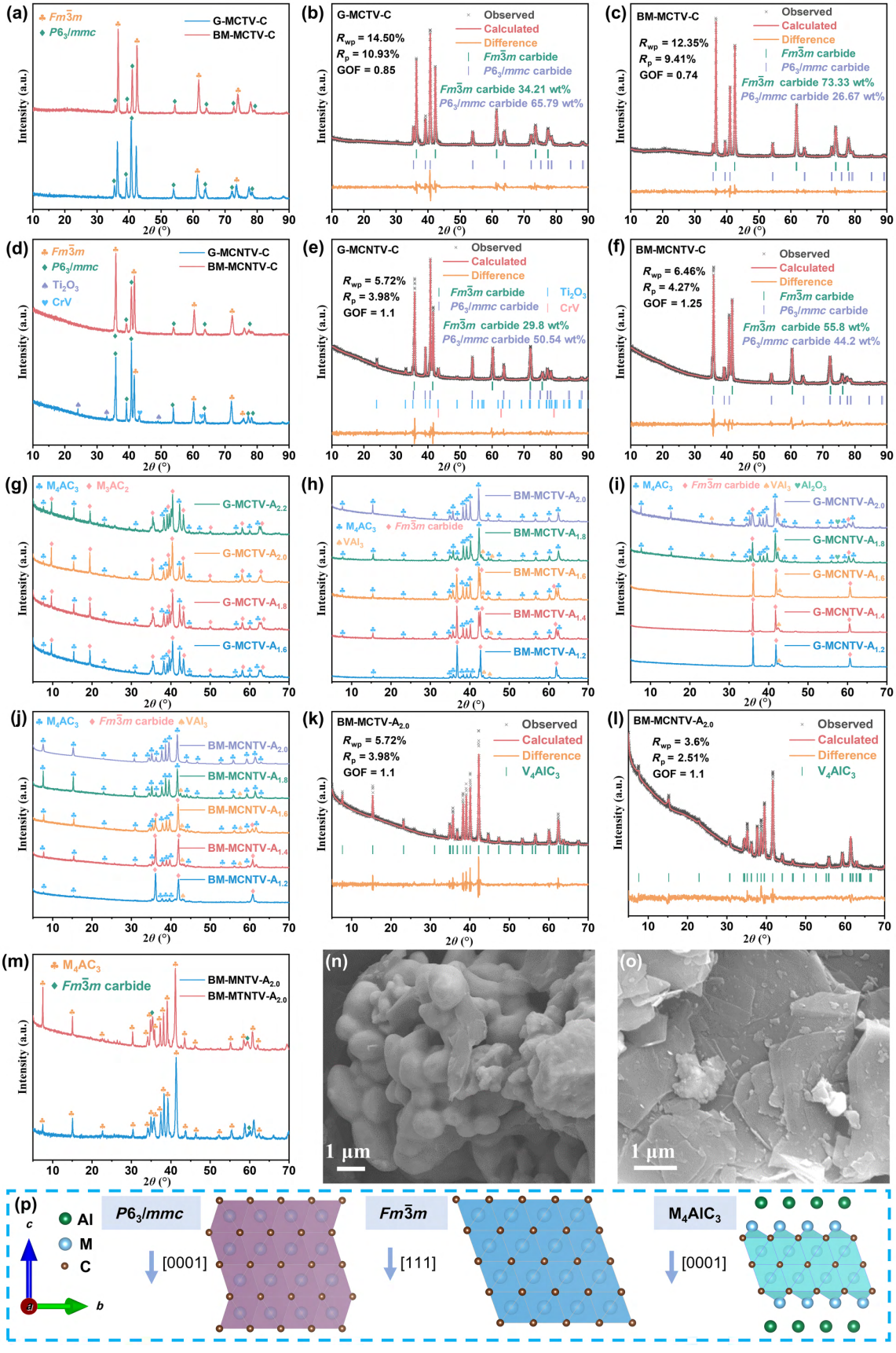

Fig. 1 (a, d) XRD patterns of MCTV-C and MCNTV-C systems obtained after calcination following grinding and ball-milling treatments, respectively. (b, c) Corresponding Rietveld refinement patterns of samples shown in (a), and (e, f) corresponding Rietveld refinement patterns of samples shown in (d). (g–j) Comparative analysis of effects of varying Al additions on synthesis of high entropy MAX under grinding and ball-milling. (k, l) Rietveld-refined XRD patterns of BM-MCTV-$A_{2.0}$ and BM-MCNTV-$A_{2.0}$. (m) XRD patterns of BM-MNTV-$A_{2.0}$ and BM-MTNTV-$A_{2.0}$. (n, o) Comparison of SEM morphologies of raw powder after different pretreatments: (n) grinding; (o) ball-milling. (p) Schematic illustration of proposed structural genetic mechanism for formation of M_4AX_3.

and BM-MCNTV-$A_{2.0}$ exhibit a significant expansion trend compared with V_4AlC_3. This expansion occurs because the larger atomic radii of Mo, Nb, and Ti atoms effectively replace the V site, resulting in noticeable lattice distortion. To further validate the universality of this synthetic strategy, we also prepared BM-MNTV-$A_{2.0}$ and BM-MTNTV-$A_{2.0}$ systems (Fig. 1(m)). The experimental results indicate that even with substantial changes in the M-position components, 413 high-quality high-entropy MAX phases can still be achieved under identical heat treatment conditions. Notably, $(Mo_{0.2}Ta_{0.2}Nb_{0.2}Ti_{0.2}V_{0.2})_4AlC_3$ was successfully synthesized via a conventional pressureless solid-state reaction route for the first time. This finding demonstrates that by regulating the dynamic pathway through the structure of carbide precursors, the component design space of the 413 high-entropy MAX phase can be effectively expanded. Since the synthesized BM-MCTV-$A_{2.0}$, BM-MCNTV-$A_{2.0}$, BM-MNTV-$A_{2.0}$, and BM-MTNTV-$A_{2.0}$ samples all exhibit typical structural features of the 413-type MAX phase, they are further simplified and denoted MCTV-MAX, MCNTV-MAX, MNTV-MAX, and MTNTV-MAX, respectively, to facilitate subsequent discussion and comparative analysis.

We characterized the microscopic morphology, component distribution, and crystal structure of the synthetic products using SEM, energy-dispersive spectroscopy (EDS), and TEM. The SEM results (Figs. 2(a)–2(d)) indicate that the four systems (MCTV-MAX, MNTV-MAX, MCNTV-MAX, and MTNTV-MAX) exhibit a pronounced layered morphology, a characteristic feature of the MAX phase. To further investigate the solid-solution states of multicomponent metal elements, we conducted EDS surface scanning analyses on these four systems (Figs. 2(a1)–2(d1)). The results demonstrate that all elements (Mo, Cr, Nb, Ti, V, Ta, and the A-site element Al) display a high degree of compositional uniformity at the micrometer scale, with no significant component segregation observed. This finding indicates that multiple transition metal elements have been successfully incorporated into the 413 MAX phase, forming a compositionally

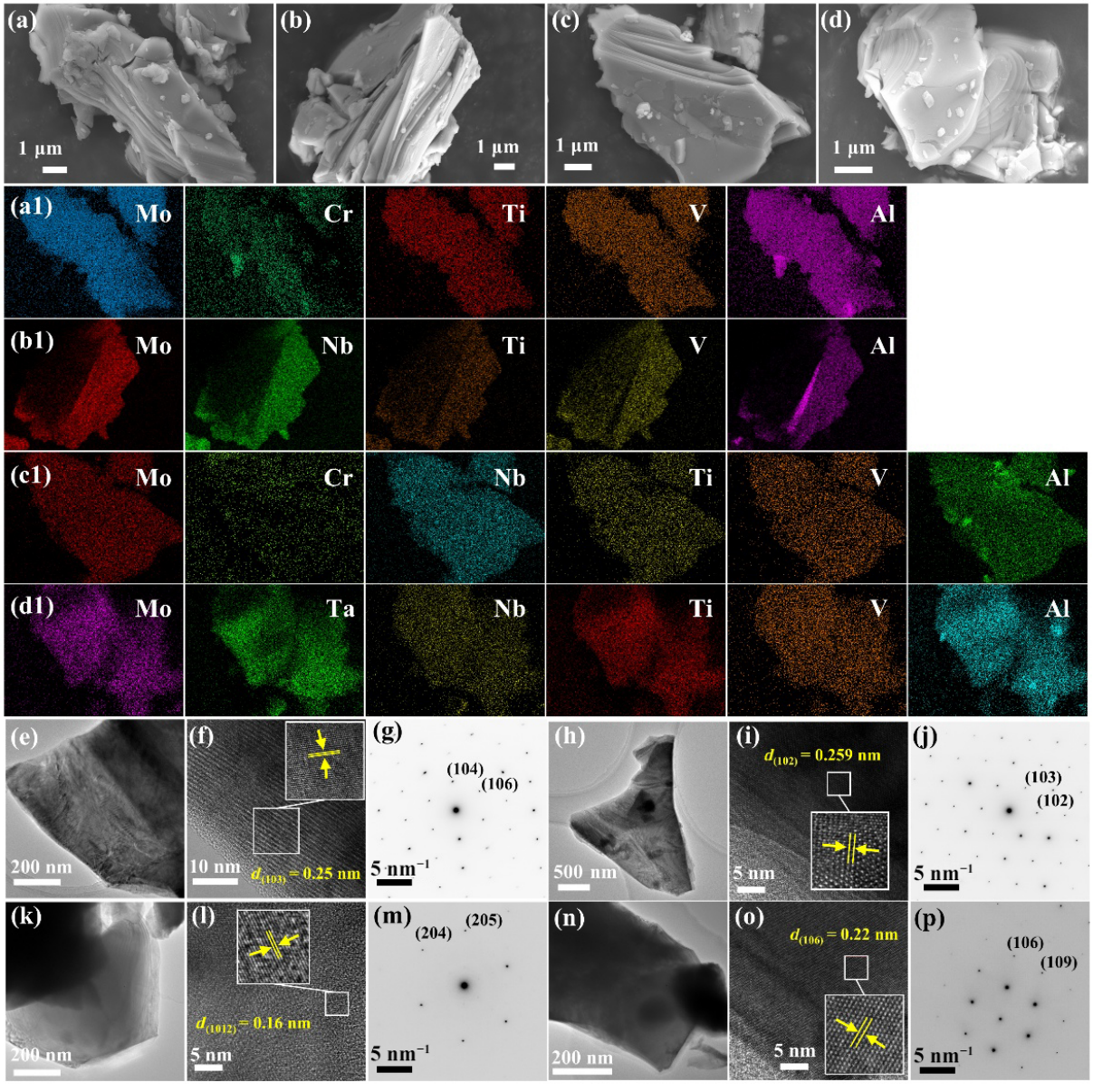

Fig. 2 (a–d) SEM images of MCTV-MAX, MNTV-MAX, MCNTV-MAX, and MTNTV-MAX; (a1–d1) EDS elemental distribution diagrams for MCTV-MAX, MNTV-MAX, MCNTV-MAX, and MTNTV-MAX; (e–g) TEM, HRTEM, and SAED images of MCTV-MAX; (h–j) TEM, HRTEM, and SAED images of MNTV–MAX; (k–m) TEM, HRTEM, and SAED images of MCNTV-MAX; (n–p) TEM, HRTEM, and SAED images of MTNTV-MAX.

homogeneous high-entropy solid solution. The HRTEM images (Figs. 2(f), 2(i), 2(l), and 2(o)) reveal periodic atomic arrangements in all four systems. The measured crystal plane spacings for each system are as follows: $d(103)$ = 0.25 nm, $d(102)$ = 0.259 nm, $d(1012)$ = 0.16 nm, and $d(106)$ = 0.22 nm. These values align closely with the lattice parameters refined by XRD Rietveld. Furthermore, the SAED diffraction patterns of each system (Figs. 2(g), 2(j), 2(m), and 2(p)) exhibit distinct diffraction spots, indicating typical hexagonal structures. The crystal planes identified in the figures, such as (104), (102), (204), and (106), fully match the structural characteristics of the 413 MAX phase. Despite significant lattice distortion from the multicomponent solid solution, the evident diffraction spots demonstrate that the material still preserves single-crystal traits, with no presence of polycrystalline rings or notable dispersion phenomena. This underscores the exceptional thermodynamic stability and structural integrity of the four high-entropy MAX phases, showcasing their ability to sustain high-quality single crystal growth even in intricate chemical environments.

To elucidate the local chemical environment of the high-entropy MAX phase and the bonding characteristics among the elements, we conducted XPS characterizations for the four systems: MCTV-MAX, MNTV-MAX, MCNTV-MAX, and MTNTV-MAX. XPS full-spectrum analysis (Fig. 3(a)) confirmed the successful presence of all metal components on the sample surface. As illustrated in Figs. 3(b)–3(e), peak fitting of the high-resolution spectra for each element revealed the distinct chemical bonding characteristics of each component. For clarity, we have marked the group diagrams of the four systems with dashed boxes in different colors. The subsequent discussion is based on this processing method. The binding energy distribution of M-position metals (Mo, Cr, Nb, Ti, V, and Ta) across each system exhibits a high degree of consistency (specific values are listed in Table 1). In the peak-division fitting analysis, the characteristic peaks at the lowest binding energy are attributed to the Al–M–C bond, providing direct evidence that the multicomponent metals have achieved cooperative bonding within the MAX phase lattice. In the high-resolution spectrum of Al 2p, the characteristic peaks observed at 72.26–72.53 eV correspond to the Al–M metallic bond in the MAX phase. Concurrently, in the C 1s spectrum, the prominent peak at 282.32–282.53 eV is associated with the C–M bond. The presence of these characteristic peaks further substantiates the formation of a strong covalent bond between M and C, as well as effective interlayer bonding with the A-position atom Al.

To evaluate the application potential of the prepared 413 high-entropy MAX phase in electromagnetic wave protection, we tested the (ε_r) and (μ_r) of the samples. Subsequently, we calculated the RL value using Eq. (1) [31]:

$$\mathrm{RL}\ (\mathrm{dB}) = 20 \lg |(Z_{\mathrm{in}} - Z_0)/(Z_{\mathrm{in}} + Z_0)| \quad (1)$$

where Z_0 is the characteristic impedance of free space, and Z_{in} is the input impedance of the absorber at the air-material interface. The RL value indicates the degree to which the incident wave is absorbed by the material. A smaller RL value corresponds to greater absorption of electromagnetic waves. The frequency range with RL < −10 dB is designated the EAB. Figure 4 presents three-dimensional (3D) reflection loss plots for four high-entropy MAX phase systems, illustrating variations with frequency and thickness, along with the corresponding two-dimensional (2D) contour plots. The research results indicate that the synergistic regulation of M-position components enables the design of absorbance characteristics, such as strong absorption, wideband, or ultrathin properties. When the matching thickness of MCTV-MAX (Figs. 4(a) and 4(b)) is 1.28 mm, $\mathrm{EAB_{max}}$ reaches 3.6 GHz (14.4–18 GHz), with an $\mathrm{RL_{min}}$ of −53.69 dB observed at a matching thickness of 1.51 mm. MNTV-MAX (Figs. 4(c) and 4(d)) demonstrates a broader EAB and the lowest RL value among the four systems. At a thickness of 1.43 mm, $\mathrm{EAB_{max}}$ extends to 3.92 GHz (13.84–17.76 GHz), while an $\mathrm{RL_{min}}$ of −59.25 dB is achieved at a thickness of 2.41 mm. MCNTV-MAX (Figs. 4(e) and 4(f)) exhibits the optimal bandwidth among the four systems. At a thickness of 1.57 mm, its $\mathrm{EAB_{max}}$ reaches 4.24 GHz (13.76–18 GHz), effectively covering most of the Ku band. Additionally, an $\mathrm{RL_{min}}$ of −52.88 dB is recorded at a thickness of 1.87 mm. MTNTV-MAX (Figs. 4(g) and 4(h)) reveals a significant advantage in thin thickness, achieving an $\mathrm{EAB_{max}}$ of 3.44 GHz at an ultrathin thickness of only 0.93 mm, with an $\mathrm{RL_{min}}$ of −51.60 dB at a thickness of 0.89 mm. The variation in the wave absorption performance clearly illustrates the "cocktail effect" associated with high-entropy materials [32]. By adjusting the types of metal elements at the M-position, we can control the wave absorption characteristics. For instance, the introduction of Ta significantly decreases the matching thickness. The performance of the present MAX phase in this experiment was compared with reported values from recent studies (Table 2). Comparative analysis indicates that the 413 high-entropy MAX phase synthesized in this study surpasses the results documented in most literature regarding $\mathrm{RL_{min}}$, $\mathrm{EAB_{max}}$, and matching thickness.

The real (ε') and imaginary part (ε'') of the dielectric constant represent the material's ability to store and dissipate electromagnetic energy, respectively [33]. As shown in Fig. 5(a), ε' for all systems decreases with increasing frequency, indicating typical frequency dispersion [34]. MTNTV-MAX exhibits a substantially higher ε' than the other systems, which indicates that it has the strongest charge-storage and polarization-response capabilities. In Fig. 5(b), ε'' for MCNTV-MAX rises markedly in the high-frequency band of 14–18 GHz, reaching a peak value of approximately 8; combined with its wide absorption bandwidth in the Ku band, this finding demonstrates that the system experiences very strong dielectric loss at high frequencies. Notably, the ε'' of MTNTV-MAX exhibited pronounced fluctuations in the 8–16 GHz band, which resulted from strong polarization resonance within the system [35]. The negative values observed at 8–10 GHz arose from interference between the induced current in the high-conductivity MAX phase under an alternating electromagnetic field and the incident field [36]. Zhang *et al.* [37] pointed out that negative imaginary permittivity may be associated with magnetoelectric coupling effects. Such negative ε'' does not violate the second law of thermodynamics because the total energy loss of the system remains positive; it is not an intrinsic dielectric property of the material but rather an electromagnetic response under specific measurement conditions. Therefore, these negative values are more appropriately understood as responses related to the sample size, electromagnetic interference, and parameter retrieval process, rather than being attributed to the intrinsic negative-loss behavior of the material. The loss-angle tangent ($\tan\delta_\varepsilon = \varepsilon''/\varepsilon'$) directly indicates how dielectric loss contributes to electromagnetic-wave attenuation. Between 13 and 18 GHz, $\tan\delta_\varepsilon$ of MCNTV-MAX increased toward 0.7, which explains why the material displayed optimal EAB in this frequency range. The high-entropy MAX phase is a typical dielectric loss material; therefore, its magnetic parameters (Fig. S2 in the ESM) will not be examined in detail. Notably, the negative value of MCNTV-MAX at high frequencies can be elucidated using Maxwell's equations. When dielectric loss is exceptionally strong, the magnetic field induced by the internal

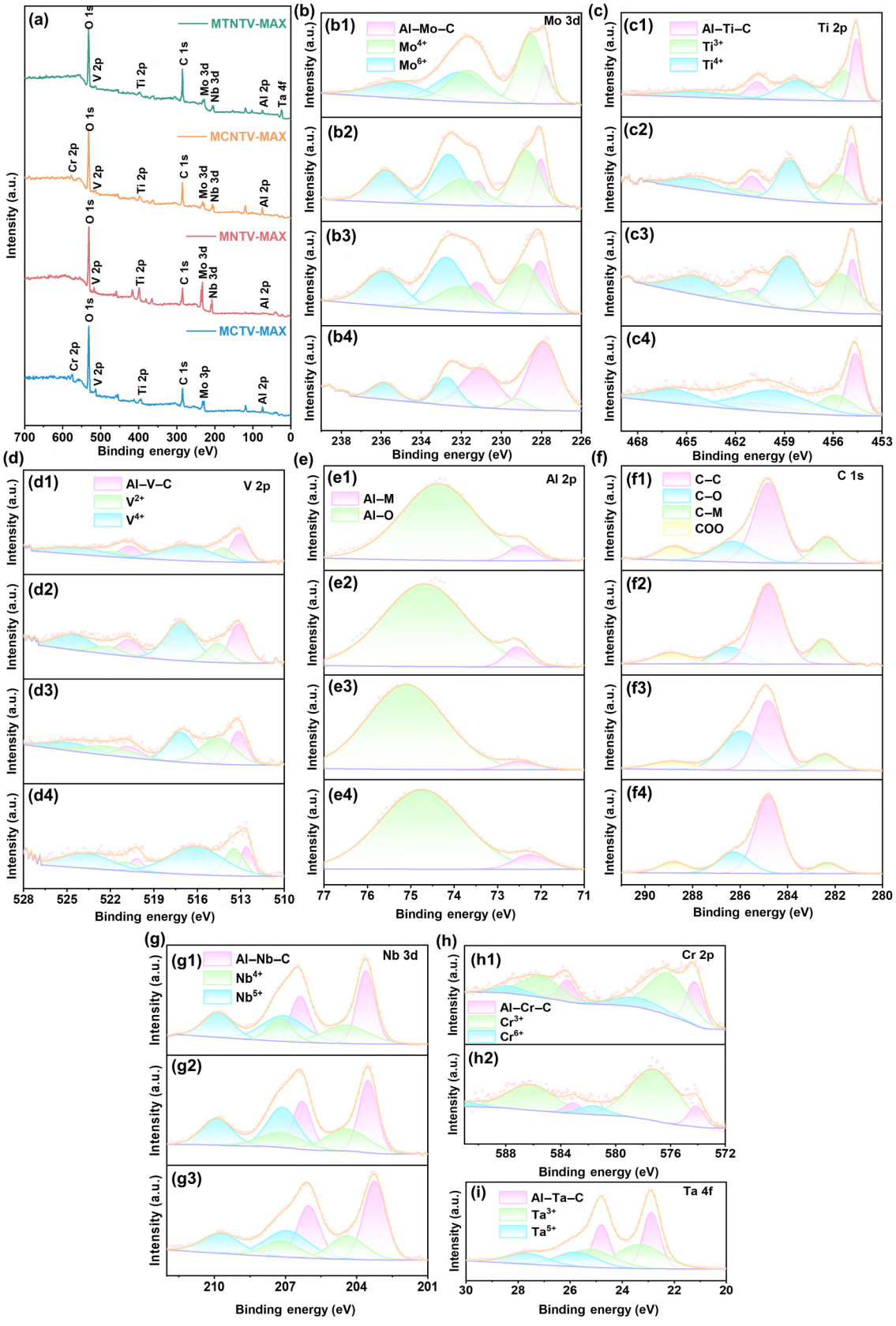

Fig. 3 (a) Full XPS spectra of MCTV-MAX, MNTV-MAX, MCNTV-MAX, and MTNTV-MAX; (b1–b4) Mo 3d spectra; (c1–c4) Ti 2p spectra; (d1–d4) V 2p spectra; (e1–e4) Al 2p spectra; and (f1–f4) C 1s spectra of MCTV-MAX, MNTV-MAX, MCNTV-MAX, and MTNTV-MAX; (g1–g3) Nb 3d spectra of MNTV-MAX, MCNTV-MAX, and MTNTV-MAX; (h1–h2) Cr 2p spectra of MCTV-MAX and MCNTV-MAX; and (i) Ta 4f spectrum of MTNTV-MAX.

alternating electric field significantly interferes with the applied magnetic field, leading to a negative equivalent magnetic parameter [25,37–39]. Similarly, this should not be attributed to the intrinsic properties of the material. The final electromagnetic

清華大學出版社 Tsinghua University Press | SciOpen

Table 1 Peak division fitting results of MCTV-MAX, MNTV-MAX, MCNTV-MAX, and MTNTV-MAX

Region	Binding energy (eV)				Assigned to
	MCTV	MNTV	MCNTV	MTNTV	
Mo 3d	227.82/230.92	228.03/231.13	228.02/231.22	227.86/231.06	Al–Mo–C
	228.52/231.72	228.73/231.93	228.92/232.02	229.26/232.36	Mo^{4+}
	232.12/235.32	232.63/235.83	232.72/235.92	232.66/235.86	Mo^{6+}
Cr 2p	574.22/583.52		574.12/583.12		Al–Cr–C
	576.32/585.32		577.22/586.02		Cr^{3+}
	578.42/587.92		581.52/590.72		Cr^{6+}
Nb 3d		203.63/206.43	203.52/206.32	203.26/206.06	Al–Nb–C
		204.43/207.23	204.42/207.22	204.36/207.16	Nb^{4+}
		207.03/209.83	207.12/209.92	206.96/209.76	Nb^{5+}
Ti 2p	454.62/460.72	454.83/460.93	454.82/460.92	454.66/460.76	Al–Ti–C
	455.32/461.92	458.63/464.23	455.52/461.42	455.76/462.16	Ti^{3+}
	458.22/464.82	455.73/461.93	458.72/464.62	459.66/465.96	Ti^{4+}
V 2p	513.12/520.72	513.13/520.73	513.12/520.72	512.56/520.16	Al–V–C
	514.22/521.82	514.53/522.23	514.52/522.32	513.46/521.06	V^{2+}
	516.82/524.72	517.13/524.63	517.12/525.12	516.06/523.76	V^{4+}
Ta 4f				22.86/24.76	Al–Ta–C
				23.26/25.26	Ta^{3+}
				25.76/27.66	Ta^{5+}
Al 2p	72.4202	72.5323	72.5232	72.2597	Al–M
	74.3202	74.7323	75.1232	74.7597	Al–O
C 1s	284.82	286.432	284.823	284.76	C–C
	286.32	284.832	285.923	286.26	C–O
	282.32	282.532	282.423	282.36	C–M
	288.82	288.932	288.923	288.86	COO

wave absorption performance of the material relies on the coordinated balance between impedance matching characteristics (Z) and attenuation capacity (α), which are calculated using Eqs. (2) and (3) [31,40], respectively:

$$Z = |Z_{in}/Z_0| = \sqrt{\frac{\mu_r}{\varepsilon_r}} \tanh\left(j\frac{2\pi fd}{c}\sqrt{\mu_r\varepsilon_r}\right) \quad (2)$$

$$\alpha = \frac{\sqrt{2}\pi f}{c} \times \sqrt{(\mu''\varepsilon'' - \mu'\varepsilon') + \sqrt{(\mu''\varepsilon'' - \mu'\varepsilon')^2 + (\mu'\varepsilon'' + \mu''\varepsilon')^2}} \quad (3)$$

where μ_r and ε_r are the complex relative permeability and complex relative permittivity of the material, respectively; f is the frequency of the electromagnetic wave; d is the thickness of the absorber; c is the speed of light in vacuum. Impedance matching serves as a prerequisite for electromagnetic waves to penetrate the interior of a material, with an ideal value of 1.0. It is widely accepted that the effective matching window ranges from 0.8 to 1.2 [25], as indicated by the area surrounded by the yellow and green lines in Figs. 5(e)–5(h). As illustrated in Figs. 5(e)–5(h), the efficient absorption regions (RL < −10 dB) of the four systems closely align with the region where $Z \approx 1$, demonstrating that optimized impedance matching is essential for achieving efficient absorption. In Fig. 5(d), the α values of all systems increase rapidly with frequency. The α value of MTNTV-MAX consistently remains the highest across the entire frequency range, exceeding 250, which demonstrates its exceptional energy dissipation potential [41]. However, the excessively high dielectric constant also results in relatively poor impedance matching, which slightly limits the effectiveness of its wave absorption. As shown in Fig. 5(o), at the thicknesses corresponding to the RL_{min} of each sample, the RL_{min} values of the four high-entropy MAX phases all appear near the frequencies where $|Z_{in}/Z_0|$ approaches 1, indicating that good impedance matching is an important prerequisite for achieving strong absorption peaks [42,43]. It should be noted that the RL_{min} only reflects the strongest absorption at a specific frequency, whereas the EAB_{max} is more dependent on sustained good impedance matching over a broad frequency range. As shown in Fig. 5(p), at the thicknesses corresponding to EAB_{max}, MCTV-MAX, MNTV-MAX, and MCNTV-MAX exhibit $|Z_{in}/Z_0|$ values close to 1 over a relatively wide frequency range, thus maintaining broad effective absorption bands. In contrast, although MTNTV-MAX possesses a relatively high α, indicating strong internal electromagnetic energy dissipation capability, the frequency range over which its $|Z_{in}/Z_0|$ value approaches 1 is relatively narrow. This suggests that its broadband impedance matching is inferior to that of the other samples, preventing its strong α from being fully converted into a broader effective absorption bandwidth. According to Debye relaxation theory, the relationship between ε' and ε'' can be described by the Cole–Cole curve (Eq. (4)) [44]:

$$\left(\varepsilon' - \frac{\varepsilon_s + \varepsilon_\infty}{2}\right)^2 + (\varepsilon'')^2 = \left(\frac{\varepsilon_s - \varepsilon_\infty}{2}\right)^2 \quad (4)$$

$$\delta(\%) = 100 \cdot \sqrt{\sum_{i=1}^{n} c_i\left(1 - \frac{r_i}{r_a}\right)^2} \quad (5)$$

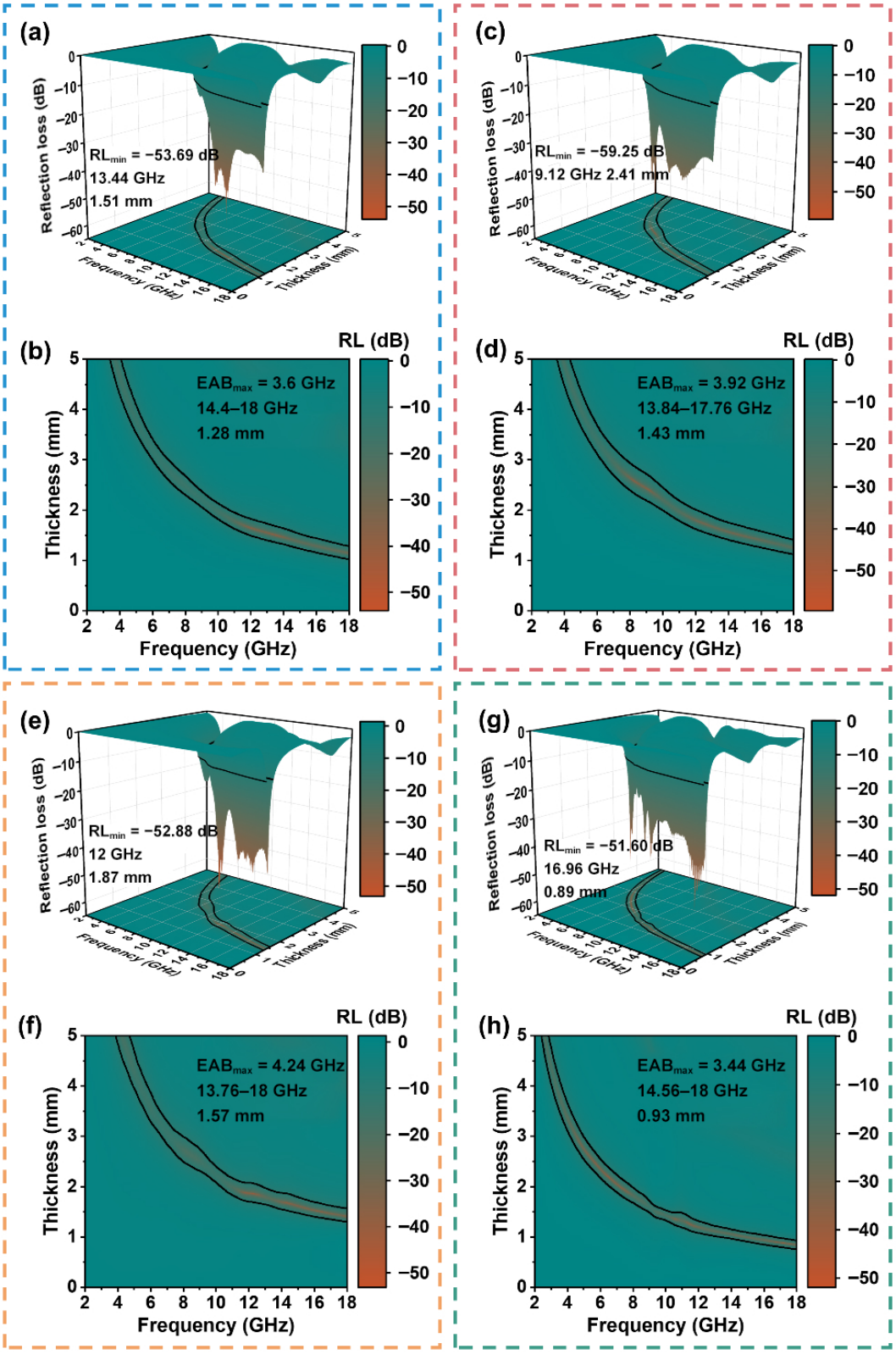

Fig. 4 Three-dimensional RL plots alongside corresponding two-dimensional contour projection plots for (a, b) MCTV-MAX, (c, d) MNTV-MAX, (e, f) MCNTV-MAX, and (g, h) MTNTV-MAX.

$$\Delta\chi_{\text{Allen}}(\%) = 100 \cdot \sqrt{\sum_{i=1}^{n} c_i \left(1 - \frac{\chi_i}{\chi_a}\right)^2} \quad (6)$$

All four systems depicted in Figs. 5(i)–5(l) exhibit multiple overlapping semicircles, each representing an independent Debye relaxation process, indicating that their losses result from multiple mechanisms [45]. For high-entropy MAX phases, the random occupation of multiple transition metal elements at the M sites leads to significant differences in atomic radius, electronegativity, and local bonding environment, thereby inducing severe lattice distortion and nonuniform charge distribution. We calculated the

Table 2 Comparison of the wave absorption performance of the high-entropy MAX phases developed in this study with findings reported in the literature

Material	RL_{min} (dB)	Thickness (mm)	EAB_{max} (GHz)	Thickness (mm)	Ref.
$(V_{1/3}Ti_{1/3}Cr_{1/3})_2AlC$	−48.01	2.22	2.96	2.50	[29]
$(Mo_{0.25}Cr_{0.25}Ti_{0.25}V_{0.25})_3AlC_2$	−45.80	1.70	3.60	1.50	[12]
$(Ti_{0.25}V_{0.25}Zr_{0.25}Nb_{0.25})_2AlC$	−62.56	2.25	3.54	2.54	[28]
$(Ti_{1/5}Nb_{1/5}Ta_{1/5}Hf_{1/5}V_{1/5})_2AlC$	−46.07	2.70	4.08	1.50	[30]
$(Ti_{0.2}Zr_{0.2}V_{0.2}Nb_{0.2}Ta_{0.2})_2AlC$	−47.00	2.40	3.92	2.78	[11]
$(Mo_{0.25}Cr_{0.25}Ti_{0.25}V_{0.25})_4AlC_3$	−53.69	1.51	3.60	1.28	This work
$(Mo_{0.25}Nb_{0.25}Ti_{0.25}V_{0.25})_4AlC_3$	−59.25	2.41	3.92	1.43	This work
$(Mo_{0.2}Cr_{0.2}Nb_{0.2}Ti_{0.2}V_{0.2})_4AlC_3$	−52.88	1.87	4.24	1.57	This work
$(Mo_{0.2}Ta_{0.2}Nb_{0.2}Ti_{0.2}V_{0.2})_4AlC_3$	−51.60	0.89	3.44	0.93	This work

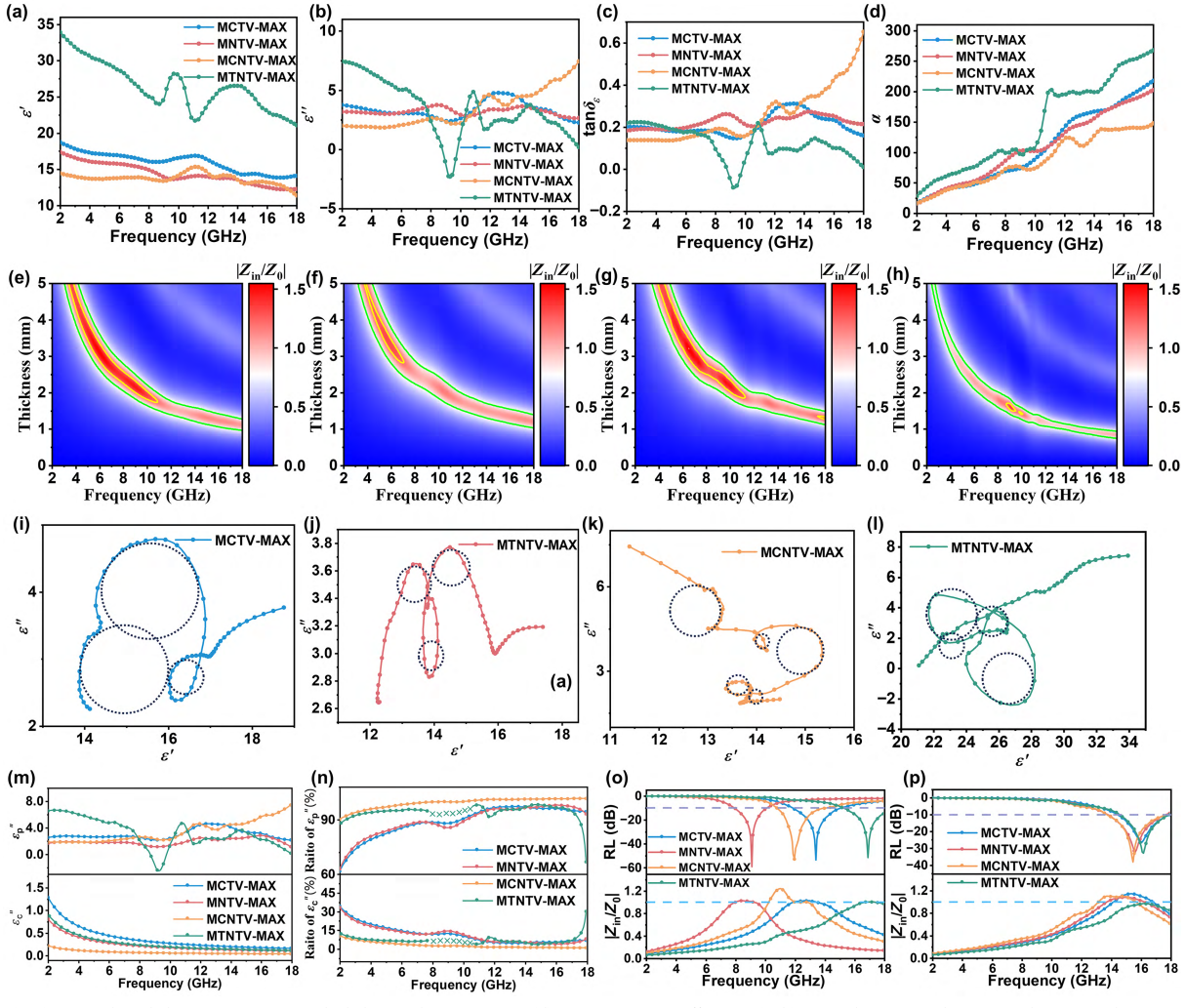

Fig. 5 (a–c) Complex dielectric constant and dielectric loss tangent, (d) attenuation coefficient, (e–h) impedance matching two-dimensional contour plot, (i–l) Cole–Cole curve, (m) degree of conduction and polarization loss, (n) ratio of ε_c'' to ε_p'', (o, p) impedance matching curves and corresponding reflection loss curves at specific thicknesses.

atomic size mismatch parameter δ and the Allen electronegativity mismatch parameter $\Delta\chi_{Allen}$ of the M-site elements according to Eqs. (5) and (6), respectively [46]. The calculated δ values of MCTV-MAX, MNTV-MAX, MCNTV-MAX, and MTNTV-MAX are 5.08%, 3.76%, 5.18%, and 3.57%, respectively, while the corresponding $\Delta\chi_{Allen}$ values are 6.51%, 3.98%, 6.45%, and 4.71%, respectively. Generally, a larger δ value indicates a more pronounced atomic size mismatch among the M-site elements, which makes the local structure of the M–C octahedra more nonuniform and more likely to form locally distorted lattice regions. A larger $\Delta\chi_{Allen}$ value suggests a greater difference in electron-attracting ability among different local M–C or M–Al bonding environments, which can easily lead to nonuniform charge distribution. These distorted lattice regions, vacancies, and other defect sites can jointly act as dipole centers, promoting dipole polarization [29,45,47–50]. In addition, abundant heterogeneous interfaces exist in the layered MAX structure, including the interfaces between the M–C sublayers and Al layers, as well as the interfaces between the MAX phase, surface oxides, and paraffin matrix. These interfaces can serve as additional

charge accumulation regions. Under an alternating electromagnetic field, the accumulated charges at these interfaces undergo periodic migration and rearrangement, thus generating interfacial polarization loss [30,51,52]. Moreover, the distorted crystal structure hinders electron transport. Electrons are scattered by the distorted lattice, leading to a shortened mean free path and reduced electrical conductivity, thereby weakening the conduction loss to some extent [53,54]. To further clarify the dielectric loss mechanism, the relative contributions of polarization loss and conduction loss were analyzed [45,47]. As shown in Fig. 5(m), the conduction loss of the four high-entropy MAX phases gradually decreases with increasing frequency. Among them, MCTV-MAX exhibits the highest conduction loss in the low-frequency region, indicating a relatively stronger conductive contribution, whereas MCNTV-MAX shows the lowest conduction loss, suggesting weakened long-range electron transport and a limited contribution from conduction loss. In contrast, polarization loss dominates over the entire frequency range and shows obvious fluctuation features in the high-frequency region, which correspond to the multiple semicircles observed in the Cole–Cole plots, indicating the existence of multiple polarization relaxation processes. As shown in Fig. 5(n), the polarization loss ratio of all four samples is higher than the conduction loss ratio over the entire frequency range. In particular, within the frequency ranges corresponding to the EAB_{max} of the samples, the polarization loss ratios exceed 90%, indicating that the microwave absorption performance of the four high-entropy MAX phases is mainly contributed by polarization loss, while conduction loss accounts for only a relatively small proportion. This result is consistent with the mechanism discussed above.

The radar cross-sectional area is a physical quantity that characterizes the intensity of the echo produced by a target when exposed to radar waves. A smaller RCS value indicates superior radar stealth performance of the material [55]. To assess the application potential of the 413 high-entropy MAX phase in real electromagnetic environments, we conducted RCS simulations using electromagnetic simulation software. The simulation model employed a PEC measuring 180 mm by 180 mm as the substrate, which was coated with a layer of optimal thickness corresponding to the system at the frequency of minimal reflection loss. The coating thicknesses for MCTV-MAX, MNTV-MAX, MCNTV-MAX, and MTNTV-MAX were 1.51, 2.41, 1.87, and 0.89 mm, respectively, and the corresponding frequencies were 13.44, 9.12, 12.00, and 16.96 GHz, respectively. Figures 6(a)–6(d) illustrate the three-dimensional far-field scattering characteristics of four high-entropy systems. In comparison with PEC plates, the scattering signal from the composite plate coated with a high-entropy MAX phase is significantly diminished, and the volume of the three-dimensional scattering sphere is notably reduced. This effect is particularly pronounced in the MCNTV-MAX system, where the reflected energy is markedly weakened. The two-dimensional polar coordinate graphs in Figs. 6(e)–6(h) further quantify this trend. In the vertically incident direction (φ = 0°), the peak intensity of the coated high-entropy MAX phase substrate is substantially lower than the reference level of the PEC substrate. This observation strongly indicates that the coating effectively converts the incident radar wave energy into thermal energy through an efficient dielectric loss mechanism. Comparing the RCS curves (Figs. 6(i)–6(l)) reveals that all systems demonstrate significant radar wave suppression effects. Notably, the RCS reductions for MCTV-MAX (18.005 dB·m²), MNTV-MAX (17.859 dB·m²), and MTNTV-MAX (15.971 dB·m²) are particularly impressive. The MCNTV-MAX system stands out with an exceptional RCS reduction of 26.2 dB·m² in the vertical

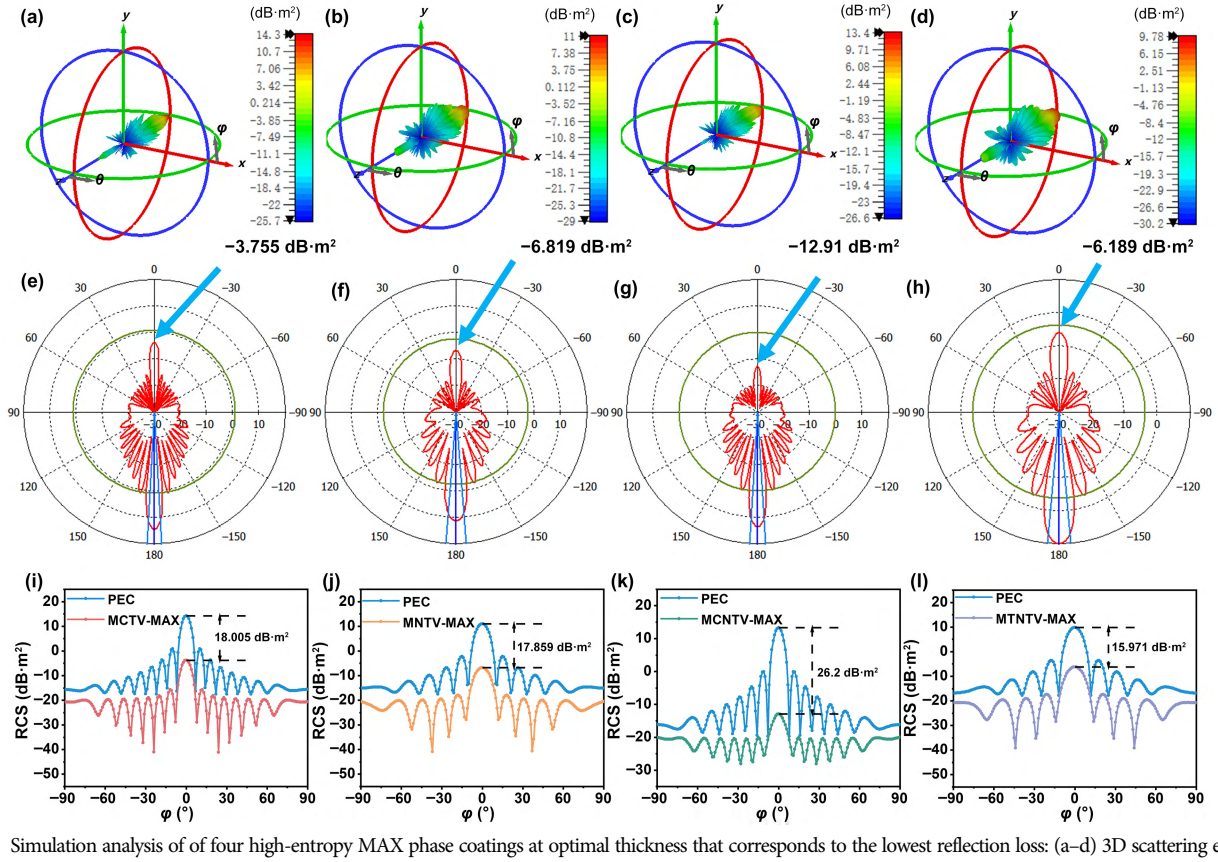

Fig. 6 Simulation analysis of of four high-entropy MAX phase coatings at optimal thickness that corresponds to the lowest reflection loss: (a–d) 3D scattering energy distribution maps, (e–h) 2D polar coordinate scattering intensity plots, (i–l) comparison curves of RCS between coated samples and PEC metal substrates.

direction (Fig. 6(k)). This simulation result aligns with its superior impedance matching and robust dielectric loss capabilities, highlighting the potential application of this series of high-entropy MAX phases in high-performance stealth coatings.

4 Conclusions

This study employed a two-step solid-state reaction to prepare the 413 high-entropy MAX phase and revealed its intrinsic formation mechanism through various pretreatment methods, demonstrating that cubic-phase carbide precursors are the key to obtaining 413 high-purity high-entropy MAX. In addition, we synthesized $(Mo_{0.2}Ta_{0.2}Nb_{0.2}Ti_{0.2}V_{0.2})_4AlC_3$ for the first time using this method and characterized it by XRD, SEM, TEM, XPS, and related techniques, providing an effective route to enrich the family of 413 high-entropy MAX-phase powders. Wave-absorption tests showed that the synthesized 413 high-entropy MAX phases all exhibited excellent absorption performance, outperforming most reported high-entropy MAX phases with respect to thickness, minimum reflection loss, and maximum effective absorption bandwidth. In particular, $(Mo_{0.2}Cr_{0.2}Nb_{0.2}Ti_{0.2}V_{0.2})_4AlC_3$ achieved an EAB_{max} of 4.24 GHz at a thickness of 1.57 mm and an RL_{min} of −52.88 dB at a thickness of 1.87 mm. $(Mo_{0.2}Ta_{0.2}Nb_{0.2}Ti_{0.2}V_{0.2})_4AlC_3$ showed a clear advantage at small thicknesses, with an EAB_{max} of 3.44 GHz and an RL_{min} of −51.5 dB at thicknesses of 0.93 and 0.89 mm, respectively. These results demonstrate the influence of the high-entropy cocktail effect on wave-absorption performance and offer a useful reference for further exploration of these materials in absorption applications.

Acknowledgements

This work was supported by the Key Research and Development Program of Shandong Province, China (No. 2023CXGC010305).

Author contributions

Chengjiao Che: formal analysis, investigation, visualization, and writing – original draft. Lintao Liu, Tan Shi, Hongyi Wang, Yiming Li, Dong Wang, and Hongyu Gong: supervision. Jianqiang Bi: conceptualization, funding acquisition, resources, and supervision. Xihua Zhang: supervision and writing – review and editing.

Availability of data and materials

The data that support the findings of this study are available from the corresponding author upon reasonable request.

Competing interests

The authors have no competing interests to declare that are relevant to the content of this article.

Electronic Supplementary Material

Supplementary material is available in the online version of this article at https://doi.org/10.26599/JAC.2026.9221350.

References

[1] Guo HT, Wang X, Pan F, *et al.* State of the art recent advances and perspectives in 2D MXene-based microwave absorbing materials: A review. *Nano Res* 2023, **16**: 10287–10325.

[2] Xu LJ, Lin ZC, Chen YJ, *et al.* Carbon-based cages with hollow confined structures for efficient microwave absorption: State of the art and prospects. *Carbon* 2023, **201**: 1090–1114.

[3] Xia QS, Han Z, Zhang ZC, *et al.* High temperature microwave absorbing materials. *J Mater Chem C* 2023, **11**: 4552–4569.

[4] Jia ZR, Lin KJ, Wu GL, *et al.* Recent progresses of high-temperature microwave-absorbing materials. *Nano* 2018, **13**: 1830005.

[5] Yao P, Qian YH, Li WC, *et al.* Exploration of dielectric and microwave absorption properties of quaternary MAX phase ceramic $(Cr_{2/3}Ti_{1/3})_3AlC_2$. *Ceram Int* 2020, **46**: 22919–22926.

[6] Zhang Z, Duan XM, Jia DC, *et al.* On the formation mechanisms and properties of MAX phases: A review. *J Eur Ceram Soc* 2021, **41**: 3851–3878.

[7] Sokol M, Natu V, Kota S, *et al.* On the chemical diversity of the MAX phases. *Trends Chem* 2019, **1**: 210–223.

[8] Zhang Y, Wen J, Zhang L, *et al.* High antioxidant lamellar structure Cr_2AlC: Dielectric and microwave absorption properties in X band. *J Alloy Compd* 2021, **860**: 157896.

[9] Zhang HB, Zhou YC, Bao YW, *et al.* Improving the oxidation resistance of Ti_3SiC_2 by forming a $Ti_3Si_{0.9}Al_{0.1}C_2$ solid solution. *Acta Mater* 2004, **52**: 3631–3637.

[10] Mellor WM, Kaufmann K, Dippo OF, *et al.* Development of ultrahigh-entropy ceramics with tailored oxidation behavior. *J Eur Ceram Soc* 2021, **41**: 5791–5800.

[11] Shen JB, Zhang M, Lin S, *et al.* High-entropy enhanced microwave absorption in MAX phases. *J Appl Phys* 2023, **133**: 235101.

[12] Qiao LJ, Bi JQ, Liang GD, *et al.* Synthesis and electromagnetic wave absorption performances of a novel $(Mo_{0.25}Cr_{0.25}Ti_{0.25}V_{0.25})_3AlC_2$ high-entropy MAX phase. *J Mater Sci Technol* 2023, **137**: 112–122.

[13] Bhalli AH, Aydinyan S, Ivanov R, *et al.* Self-propagating high-temperature synthesis as an enabling route for high-entropy MAX phases. *Materials* 2026, **19**: 1829.

[14] Zhang J, Jia R, Tan KB, *et al.* A review of MAX series materials: From diversity, synthesis, prediction, properties oriented to functions. *Nano-Micro Lett* 2025, **17**: 173.

[15] He HJ, Hu BT, Soomro SA, *et al.* Synthesis, microstructure, physical and mechanical properties of phase-pure entropy-enhanced $(Nb_{0.8}Ti_{0.05}Ta_{0.05}V_{0.05}M_{0.05})_4AlC_3$ (M = Hf, Zr) ceramics. *J Eur Ceram Soc* 2023, **43**: 5782–5791.

[16] Du ZG, Wu C, Chen YC, *et al.* High-entropy atomic layers of transition-metal carbides (MXenes). *Adv Mater* 2021, **33**: 2101473.

[17] Xiao H, Zhao S, Liu QY, *et al.* Point defect properties in high entropy MAX phases from first-principles calculations. *Acta Mater* 2023, **248**: 118783.

[18] Tunca B, Huang SG, Goossens N, *et al.* Chemically complex double solid solution MAX phase-based ceramics in the (Ti,Zr,Hf,V,Nb)–(Al,Sn)–C system. *Mater Res Lett* 2022, **10**: 52–61.

[19] Zou HR, Zhang JY, Ren L, *et al.* Microstructure mechanical properties and tribological properties of high entropy M_2AlC–MC (M = Ti, V, Zr, Hf, Ta) composites prepared via spark plasma sintering. *J Eur Ceram Soc* 2024, **44**: 1421–1428.

[20] Bao WC, Wang XG, Ding HJ, *et al.* High-entropy M_2AlC–MC (M = Ti, Zr, Hf, Nb, Ta) composite: Synthesis and microstructures. *Scripta Mater* 2020, **183**: 33–38.

[21] Ma K, Shi XG, He GQ, *et al.* *In situ* reaction synthesis, microstructure and thermomechanical properties of novel medium-entropy $(Ti,V,Nb,Ta)_2AlC$ ceramics. *Ceram Int* 2023, **49**: 21206–21212.

[22] Cao L, Zhang QQ, Du LJ, *et al.* Synthesis and characterization of high entropy $(TiVNbTaM)_2AlC$ (M = Zr, Hf) ceramics. *J Adv Ceram* 2024, **13**: 237–246.

[23] Zou HR, Zhang W, Zhang JY, *et al.* Synthesis of a novel textured high entropy M_4AlC_3 (M = Ti, V, Mo, Nb, Ta) composites with improved mechanical properties via spark plasma sintering. *J Eur Ceram Soc* 2024, **44**: 6889–6900.

[24] Nemani SK, Zhang BW, Wyatt BC, *et al.* High-entropy 2D carbide MXenes: $TiVNbMoC_3$ and $TiVCrMoC_3$. *ACS Nano* 2021, **15**: 12815–12825.

[25] Qiao LJ, Bi JQ, Liang GD, *et al.* Synthesis of high-entropy MXenes

with high-efficiency electromagnetic wave absorption. *J Adv Ceram* 2023, **12**: 1902–1918.
[26] Wyatt BC, Yang YN, Michałowski PP, *et al.* Order-to-disorder transition due to entropy in layered and 2D carbides. *Science* 2025, **389**: 1054–1058.
[27] Zhang H, Hu T, Wang XH, *et al.* Discovery of carbon-vacancy ordering in Nb_4AlC_{3-x} under the guidance of first-principles calculations. *Sci Rep* 2015, **5**: 14192.
[28] Wang SQ, Miao BJ, Nadeem MS, *et al.* Preparation and microwave absorption performance study of high-entropy MAX phase $(Ti_{1/4}V_{1/4}Zr_{1/4}Nb_{1/4})_2AlC$. *Ceram Int* 2025, **51**: 23760–23771.
[29] Luo W, Liu Y, Wang CY, *et al.* Molten salt assisted synthesis and electromagnetic wave absorption properties of $(V_{1-x-y}Ti_xCr_y)_2$ AlC solid solutions. *J Mater Chem C* 2021, **9**: 7697–7705.
[30] Liu JL, Wang L, Huang MQ, *et al.* Surface magnetic regulation in carbon microspheres induced by melamine to increase electromagnetic wave absorption. *J Adv Ceram* 2025, **14**: 9221200.
[31] Pang HF, Duan YP, Huang LX, *et al.* Research advances in composition, structure and mechanisms of microwave absorbing materials. *Compos Part B—Eng* 2021, **224**: 109173.
[32] Liu D, Deng YJ, Zhang XZ, *et al.* Deciphering mechanism of cocktail effect in high-entropy alloy catalysis. *Adv Mater* 2026, **38**: 72971.
[33] Li M, Zhang Y, Chen ZH, *et al.* A simple co-doping strategy to synthesis of Ni@B/N carbon nanotubes with broadband and low-frequency electromagnetic wave absorption. *Chem Eng J* 2024, **483**: 149151.
[34] Feng SX, Wang HW, Ma J, *et al.* Fabrication of hollow Ni/NiO/C/MnO_2@polypyrrole core–shell structures for high-performance electromagnetic wave absorption. *Compos Part B—Eng* 2024, **275**: 111344.
[35] Zhang K, Liu Y, Li X, *et al.* All-dielectric ultra-broadband microwave absorbing aerogel with optimized dielectric dispersion via dielectric relaxation time regulation. *Adv Mater* 2025, **37**: 2506386.
[36] Hou ZL, Zhang M, Kong LB, *et al.* Microwave permittivity and permeability experiments in high-loss dielectrics: Caution with implicit Fabry–Pérot resonance for negative imaginary permeability. *Appl Phys Lett* 2013, **103**: 162905.
[37] Zhang KL, Hou ZL, Kong LB, *et al.* Origin of negative imaginary part of effective permittivity of passive materials. *Chinese Phys Lett* 2017, **34**: 097701.
[38] Liu DW, Du YC, Li ZN, *et al.* Facile synthesis of 3D flower-like Ni microspheres with enhanced microwave absorption properties. *J Mater Chem C* 2018, **6**: 9615–9623.
[39] Zhao HB, Fu ZB, Chen HB, *et al.* Excellent electromagnetic absorption capability of Ni/carbon based conductive and magnetic foams synthesized via a green one pot route. *ACS Appl Mater Inter* 2016, **8**: 1468–1477.
[40] Du B, Wang SD, Guo LW, *et al.* Design and fabrication of $(Hf_{0.25}Zr_{0.25}Ta_{0.25}Nb_{0.25})C$–SiC ceramics with improved microwave absorbing properties via PDC route. *J Adv Ceram* 2025, **14**: 9220998.
[41] Shu RW, Wan ZL, Zhang JB, *et al.* Facile design of three-dimensional nitrogen-doped reduced graphene oxide/multi-walled carbon nanotube composite foams as lightweight and highly efficient microwave absorbers. *ACS Appl Mater Inter* 2020, **12**: 4689–4698.
[42] Yu GY, Shao GF, Xu ZL, *et al.* Hierarchical interface-engineered magnetic graphene–SiCN aerogels via a stepwise confinement strategy for low-frequency and broadband microwave absorption. *J Adv Ceram* 2025, **14**: 9221187.
[43] Shao GF, Xu RP, Chen Y, *et al.* Miniaturized hard carbon nanofiber aerogels: From multiscale electromagnetic response manipulation to integrated multifunctional absorbers. *Adv Funct Mater* 2024, **34**: 2408252.
[44] He M, Chen H, Peng H, *et al.* Ultralight $Ti_3C_2T_x$-derivative chrysanthemum-like $Na_2Ti_3O_7/Ti_3C_2T_x$ MXene quantum dots 3D/0D heterostructure with advanced microwave absorption performance. *Chem Eng J* 2023, **456**: 140985.
[45] Cui RP, Li Y, Zhang XF, *et al.* Controlled deintercalation of graphene /organic superlattices with dense atomic-scale steric Schottky heterojunctions for extreme microwave absorption. *Nat Commun* 2025, **16**: 5804.
[46] Poletti MG, Battezzati L. Electronic and thermodynamic criteria for the occurrence of high entropy alloys in metallic systems. *Acta Mater* 2014, **75**: 297–306.
[47] Cui RP, Duan ZW, Li Y, *et al.* High-temperature oxide ceramic microwave absorber enabled by thermionic migration mediated by electron delocalization. *Nat Commun* 2025, **16**: 9179.
[48] Zhao B, Du YQ, Yan ZK, *et al.* Structural defects in phase-regulated high-entropy oxides toward superior microwave absorption properties. *Adv Funct Mater* 2023, **33**: 2209924.
[49] Zhao B, Yan ZK, Du YQ, *et al.* High-entropy enhanced microwave attenuation in titanate perovskites. *Adv Mater* 2023, **35**: 2210243.
[50] Zhao B, Yan ZK, Liu LL, *et al.* A liquid-metal-assisted competitive galvanic reaction strategy toward indium/oxide core–shell nanoparticles with enhanced microwave absorption. *Adv Funct Mater* 2024, **34**: 2314008.
[51] Zhao B, Du YQ, Lv HL, *et al.* Liquid-metal-assisted programmed galvanic engineering of core–shell nanohybrids for microwave absorption. *Adv Funct Mater* 2023, **33**: 2302172.
[52] Du YQ, Yan ZK, You WB, *et al.* Balancing MXene surface termination and interlayer spacing enables superior microwave absorption. *Adv Funct Mater* 2023, **33**: 2301449.
[53] Aamlid SS, Oudah M, Rottler J, *et al.* Understanding the role of entropy in high entropy oxides. *J Am Chem Soc* 2023, **145**: 5991–6006.
[54] Gild J, Samiee M, Braun JL, *et al.* High-entropy fluorite oxides. *J Eur Ceram Soc* 2018, **38**: 3578–3584.
[55] Yang YF, Xu DM, Kong LX, *et al.* Construction of Ni–Zn bimetal sulfides heterostructured-hybrids for high-performance electromagnetic wave absorption. *J Colloid Interf Sci* 2022, **606**: 1410–1420.